DEVELOPING A CONTROL STRATEGY FOR CARNOT BATTERIES: ANALYSIS OF TEMPERATURE GLIDE EFFECTS IN ORGANIC RANKINE CYCLE AND HEAT PUMP MODES

Aitor Cendoya[1]*, Frederic Ransy[1], Olivier Dumont[1], Bentao Guo[1], Vincent Lemort[1]

[1]Thermodynamics Laboratory, Faculty of Applied Sciences, University of Liege, Liege, Belgium

*Corresponding Author: acendoya@uliege.be

ABSTRACT

Energy storage is a critical technology to integrate renewable energy into the power grids successfully and has been widely recognised as essential for the energy transition. Carnot Batteries (CBs) offer a promising solution for long-duration energy storage by integrating thermal energy storage and power cycles. This study investigates the impact of temperature glide on the evaporator and condenser of a CB system designed to produce 50 kWe and 500 kWth. A physics-based model is developed, incorporating manufacturer data to accurately reflect real performance. The analysis evaluates system efficiency in both organic Rankine cycle (ORC) and heat pump (HP) modes, considering the component limitations. The results indicate that no single temperature glide pair optimises performance in both operational modes. Instead, the optimal glide values vary depending on the operating conditions. This highlights the importance of conducting detailed analyses, particularly when secondary fluid circuits are shared between modes, as significantly different operating conditions can arise. Consequently, implementing a mode- and condition-dependent control strategy is essential for maintaining high efficiency in CBs. Additionally, this study identifies the optimal temperature glides for the analysed system, demonstrating their dependence on piping, fittings, and component selection.

1 INTRODUCTION

Currently, fossil fuels account for more than 65% of the global energy mix (Ritchie et al., 2024), while the remaining share is derived from renewable energy sources (RES). This percentage is expected to increase three times by 2030 in order to mitigate the global warming effect on humanity (International Energy Agency (IEA), 2024). However, this is not free from challenges, RES are inherently variable and subject to fluctuations, leading to imbalances between energy production and end-user demand (Hodge et al., 2018). A key strategy to enhance the share of RES in the electricity grid is the implementation of storage technologies, which play a crucial role in the energy transition by mitigating supply-demand mismatches (Vecchi et al., 2022).

Short-term storage is primarily managed through electrical and electrochemical batteries, nevertheless, these technologies face constraints related to raw material availability and limited lifespan (Dehghani-Sanij et al., 2019). In contrast, long-term energy storage remains a significant challenge. In some cases, sensible heat storage is integrated to absorb surplus energy from RES and store it in the form of heat, reducing primary energy consumption in buildings. These systems can achieve high renewable energy self-consumption ratios (Ahmadfard & Baniasadi, 2025; Cendoya et al., 2024a). However, they have not yet been able to provide electricity. One approach to address this limitation is the integration of a heat-to-power cycle, which enables electricity generation. Combined with a heat pump cycle, this system is called Carnot Battery (CB). This technology is particularly promising as it is not constrained by geographical location or raw material availability.

This technology has the potential to integrate multiple energy sources into a single system (Cendoya et al., 2024b), enabling connection to District Heating Networks (DHN), where they can provide heating and cooling to various end-users while also generating electricity based on demand. CBs are composed of two cycles, one power-to-heat and one heat-to-power, in which the technology can vary depending

on the boundary conditions. Moreover, this technology can be coupled with different storage solutions, such as phase change materials (PCM), silica-based storage (McTigue et al., 2025), or ice storage (Guo et al., 2025). Several prototypes of CB have already been tested by researchers, mainly with the integration of Organic Rankine Cycles (ORC), demonstrating that the heat-to-power cycle presents relatively low performance while exhibiting promising Round Trip Efficiency (RTE). However, there are still several challenges associated with the development of these systems, related to their control in both modes. Furthermore, these technologies show particularly interesting performance when combined with low-temperature waste heat, enhancing the overall efficiency of the system. Additionally, by integrating various components, it is possible to reduce investment costs, as key components are shared (Daniarta et al., 2024).

This paper presents a control map for the secondary fluid loop in a CB system, developed within the WeForming project to deliver 50 kWe of electricity and 500 kWth of heating power. The system shares nearly all components, except for the expander and compressor, which are dedicated to the ORC and Heat Pump (HP), respectively. Optimising the temperature glide between the working fluid and the secondary fluid is crucial, as a trade-off exists between secondary pump energy consumption and system performance. This work aims to propose a control map for the operation of secondary fluids in reversible heat exchangers and piping circuits for CB. The effect is assessed through numerical modelling, which is validated against manufacturer data from off-the-shelf components.

2 Methodology

This section provides a detailed overview of the case study, focusing on its role and the integration of the CB. Additionally, it presents a summary of the system component modelling and validation, along with a more detailed discussion of the secondary fluid equations and their impact on overall performance.

2.1 Case study explanation

In past decades, several mines across Europe have been closed as they became increasingly unprofitable and were closed and abandoned. Nowadays, it is estimated that approximately 11000 of these former mining sites are flooded (Pinto et al., 2020), representing a significant opportunity for large-scale thermal energy storage. The case study analyses the integration of the CB with an abandoned slate mine in Martelange, a town on the border between Belgium and Luxembourg. The mine is flooded with 500000 m³ of water, which can be used to store energy. Surrounding the mine is a residential area with high energy demands for space heating and domestic hot water. Currently, these buildings rely on independent heat pumps, which are planned to be replaced by a district heating network (DHN). Figure 1 presents the schematic of the case study, which is expected to be completed by early 2026. This figure additionally presents the interaction between a 70 kWe photovoltaic (PV) system and a 140 kWth photovoltaic-thermal (PT) collector installation. The PTs are connected to a water circuit to be stored in the medium-high temperature underground storage, to then feed the CB-ORC preheater or the CB-HP evaporator. This storage, in particular, aims to represent the potential of low-temperature waste heat, which can be found in several industrial processes. Moreover, the system can utilise the surplus electricity from the grid for different purposes.

The study site includes multiple storage options:

- Medium-low-temperature storage (25–45°C): A 6000 m³ underground storage volume, which is coupled to a fourth-generation district heating network to cover the heat demand of existing buildings.
- Medium-high-temperature storage (40–60°C): A 600 m³ underground storage volume, with temperature limitations dictated by the operating conditions of submersible pumps, this storage is used in the CB operation.
- Low-temperature storage (10–20°C): A 20000 m³ chamber, where the ORC condenser will reject the heat. In parallel, this heat will then be released into the medium and is not expected to overheat the cold sink.

- High-temperature storage (80-115): A 20 m³ insulated water tank located overground, designated for storing the high-temperature energy required for ORC evaporator operation.

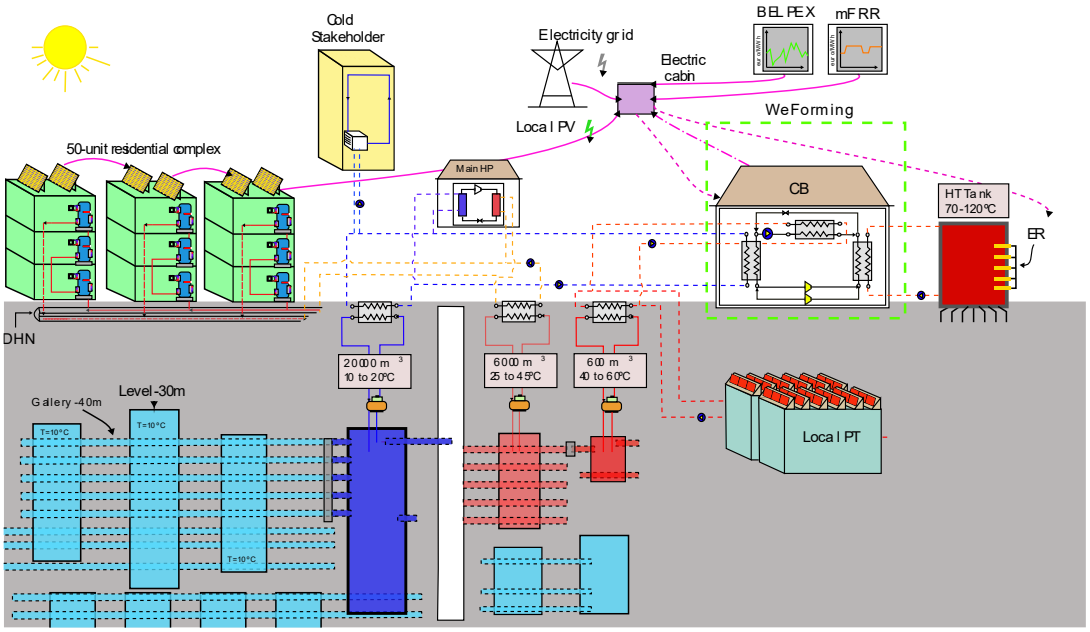

Figure 1: Schematic representation of the CB and the integration with the study site

The CB is designed to generate 50 kWe in the expander, operating with a water supply temperature of 100°C in the evaporator ($T_{w,su,ev}$) and 15°C in the condenser ($T_{w,su,cd}$). In addition, 50°C water feeds the preheater ($T_{w,su,pre}$), this exchange represents a waste heat source (the energy comes from the medium-high-temperature storage). In HP mode, the system is designed to produce 500 kWth, supplied by water at 50°C in the HP evaporator and producing hot water at 95°C in the condenser. In the system, off-the-shelf components have been selected to ensure reliability and efficiency. The key components include:

- Expander: HSEL8591-110Y-40 semi-hermetic screw-type from Bitzer, used in the ORC cycle.
- Compressor: CSH2T9573-240Y-35D compact screw type from Bitzer, responsible for refrigerant circulation in HP mode
- Pump: Low-NPSH centrifugal pump (ICP2/32-185) from Verder for the ORC mode
- Heat Exchangers: Brazed Plate Heat Exchangers from Alfa Laval are shared in both modes, models CB410-200M, CBH210-170AH and CB210-60, for condenser, evaporator and preheater in ORC mode.

These components were chosen to optimise system performance and ensure compatibility with the thermal storage and energy conversion processes. The working fluid corresponds to R1233ZD(E) and the secondary fluid to pressurised water, both chosen for their high performance in high-temperature applications and their availability, respectively.

2.2 Modelling

The machine modelling is divided into two main sub-sections. The first section focuses on the CB itself, providing a concise explanation of the modelling approach along with its validation and representation. The second section details the key equations used to analyse secondary fluid effects.

2.2.1 CB Modelling: The CB system is modelled using numerical representations of its components, aiming to capture all relevant physical phenomena associated with the refrigerant, secondary fluid and components. Except for the compressor, the modelling of the CB has been previously documented in (Cendoya et al., 2024c). Table 1 presents a summary of the different modelled CB components within their respective references and the correlation employed for the Heat Transfer Coefficient (HTC), pressure drops and refrigerant charge computation. Moreover, the accuracy of each model against the

manufacturer's data is presented. These models are integrated into Python using a modular approach, in which thermodynamic properties are obtained from the CoolProp library (Bell et al., 2014). The numerical convergence of the system is achieved using the root iterative method, available in Scipy (Virtanen et al., 2020), which aims to minimise the numerical residuals of each component by adjusting the initial guesses.

Table 1: Summary of the CB modelling.

Component	Model	Correlations	Validation Error
Condenser ORC / Evaporator HP	(Cuevas et al., 2009): Heat exchanger discretised according to the different refrigerant phases. Superheated, two-phase and subcooling.	**HTC:** Single phase (Holger Martin, 2010) Condensation, (Shah, 2021) Boiling, (Amalfi et al., 2016a) **Pressure Drop:** Single phase, (Holger Martin, 2010) Condensation, (Longo, 2010) Boiling, Amalfi et al. (2016) and (Amalfi et al., 2016b) **Charge:** (Cioncolini & Thome, 2012)	**ORC:** ±0.41% for the heat Power, ±3.20% for the pressure drops, and ±1.12°C for the exhaust temperature **HP:** ±2.98% for the heat Power, ±5.90% for the pressure drops, and ±1.51°C for the exhaust temperature
Evaporator ORC / Condenser ORC	(Cuevas et al., 2009)): Heat exchanger discretised according to the different refrigerant phases. Superheated, two-phase and subcooling.	**HTC:** Single phase (Holger Martin, 2010) Condensation, (Shah, 2021) Boiling, (Amalfi et al., 2016a) **Pressure Drop:** Single phase, (Holger Martin, 2010) Condensation, (Longo, 2010) Boiling, Amalfi et al. (2016) and (Amalfi et al., 2016b) **Charge:** (Cioncolini & Thome, 2012)	**ORC:** ±1.76% for the heat Power, ±0.05% for the pressure drops, and 0.2°C for the exhaust temperature **HP:** ±0.57% for the heat Power, ±0.40% for the pressure drops, and ±1.22°C for the exhaust temperature
Expander	(Lemort et al., 2012): A semi-empirical model capable of accounting for over- and under-expansion phenomena, as well as refrigerant leakages, electromechanical losses, and internal heat transfer effects.	/	Number of manufacturer points: 18. The errors correspond to ±5% for the power, ±5% for the refrigerant mass flow rate, and ±6K for the exhaust temperature.
Compressor	(Cuevas et al., 2010): A semi-empirical model capable of accounting for over- and under-compression phenomena. Additionally, refrigerant leakages, electromechanical losses, and internal heat transfer effects are considered.	/	Number of manufacturer points: 275. The errors correspond to ±5% for the power, ±5% for the refrigerant mass flow rate, and ±3K for the exhaust temperature.
ORC-pump	(Eck, 1973): Dimensionless factors (power, flow, and pressure) are used to predict the performance and behaviour of pumps and fans.	/	The R^2 for the factors' curve fit based on the pressure factor is 99.5% and 97.6% for the flow factor and power factor, respectively.
Pre-heater	(Cuevas et al., 2009): Heat exchanger discretised according to the different refrigerant phases. Single-phase, and there may be the possibility of two-phase.	**HTC:** Single phase (Holger Martin, 2010) Boiling, (Amalfi et al., 2016a) **Pressure Drop:** Single phase, (Holger Martin, 2010) Boiling, Amalfi et al. (2016) and (Amalfi et al., 2016b) **Charge:** (Cioncolini & Thome, 2012)	**ORC:** ±3.31% for the heat Power, ±7.7% for the pressure drops, and ±0.1°C for the exhaust temperature

2.2.2 Secondary Fluid Loop: This study focuses on determining the optimal glide for the secondary fluid. To achieve this, it is essential to consider not only the modelling of the CB but also the pressure drops that must be overcome for the secondary fluid in the piping to effectively transfer heat to the refrigerant. Three different water circuits are analysed (all considering the same medium):

- Circuit 1 (c_1): Corresponds to the high-temperature circuit, supplying heat to the evaporator in the ORC mode and to the condenser in the HP mode.
- Circuit 2 (c_2): Represents the low-temperature circuit, which feeds the condenser in ORC mode.
- Circuit 3 (c_3): Corresponds to the medium-temperature circuit, supplying heat to the preheater in ORC mode and to the evaporator in HP mode.

Figure 2 represents these circuits and their interactions within the system. Pressure drops arise from two main sources: (1) the brazed plate heat exchangers, which are modelled through CB correlations, and (2) the pressure losses in the piping system.

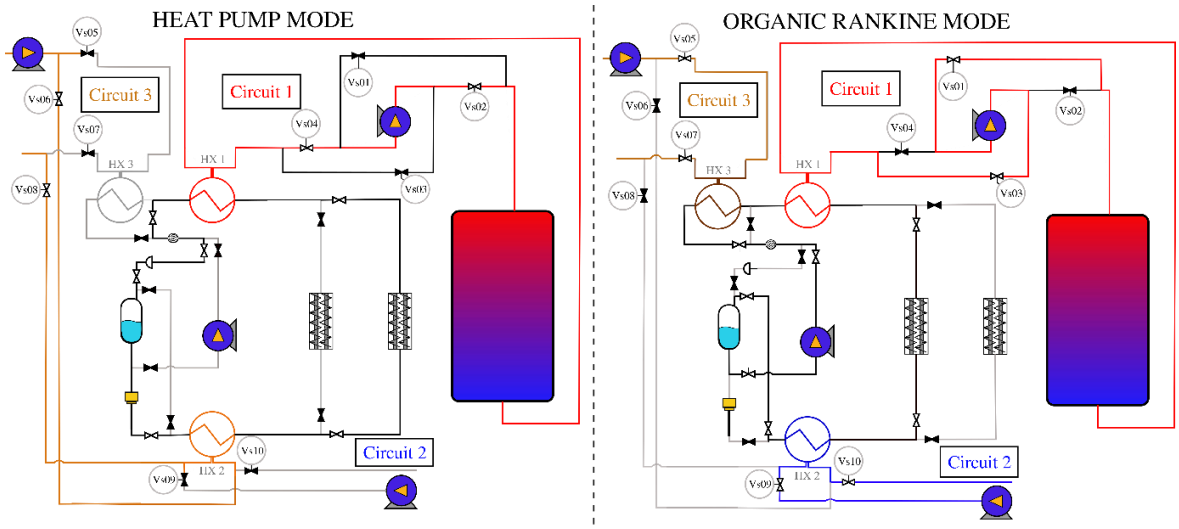

Figure 2: P&ID of the analysed system HP mode (left) and ORC mode (right)

These pressure drops have a direct impact on the overall energy consumption of the system. To compute the pressure drop in the brazed plate heat exchangers (ΔP_{hx}), the correlation proposed by (Holger Martin, 2010) is employed, considering water in a single-phase (liquid) state. The set of equations employed to compute the pressure drops is presented in equations 1 and 2. The equations depend on geometrical parameters of the heat exchangers: length of the plate ($L_{p,hx}$) and the hydraulic diameter ($D_{hyd,hx}$). Moreover, viscosity (μ_w) and density (ρ_w) are computed at the average water conditions.

$$\Delta P_{hx} = Hg \cdot \frac{\mu_w^2 \cdot L_{p,hx}}{\rho_w \cdot D_{hyd,hx}^3} \quad (1)$$

$$Hg = f_{hx} \cdot \frac{Re^2}{2} \quad (2)$$

The Hagen number is computed through the Reynolds number (Re) and the friction factor (f_{hx}), which is determined using the correlation proposed by Holger (Martin, 1996). This approach has been validated against manufacturer data, yielding an error of less than 5%. The second major contributor to pressure losses is the piping system, which includes both frictional (ΔP_f) and minor losses (ΔP_m). Frictional pressure drops are calculated using the Darcy-Weisbach equation, which relies on the piping length (L_{pip}), diameter (D_{pip}) and the fluid speed (C_{pip}).

$$\Delta P_f = f \cdot L_{pip}/D_{pip} \cdot \rho_w \cdot C_{pip}^2/2 \quad (3)$$

The friction factor (f) is determined based on the Re, for laminar regimen (Re<2100), it follows the relation $f = 64/Re$. For transitional and turbulent regimes, the Colebrook-White equation is applied, which accounts for pipe roughness (Kast et al., 2010). Minor pressure losses arise from flow disturbances caused by fittings such as elbows, valves, and tee junctions, as well as changes in cross-sectional area. These losses are quantified using equation 4. The minor pressure loss coefficients (k_v, i) are extracted from the reference, Kast et al., (2010). In addition, minor pressure in the inlet ($k_{v,in}$) and outlet ($k_{v,ex}$) of the piping is considered.

$$\Delta P_m = (k_{v,in} + \sum k_{v,i} + k_{v,ex}) \cdot (\rho_w \cdot C_{pip}^2/2) \quad (4)$$

The energy consumption of the pump ($\dot{W}_{pp,sf,}$) circulating the secondary fluid is computed using Equation 5, which considers the water mass flow rates ($\dot{M}_w$) and the total pressure drops (ΔP_t). In addition, both isentropic (η_{is}) and mechanical efficiencies (η_m) are considered in the energy balance.

$$\dot{W}_{pp,i,sf} = \dot{M}_{w,ci} \cdot \frac{1/\rho_{w,ci} \cdot (\Delta P_{t,ci})}{\eta_{is} \cdot \eta_m} \quad (5)$$

Table 2 presents the main fitting components and their respective distances. The piping system consists of DN100 carbon steel pipes, arranged as shown in Figure 2, and designed to operate in both modes. Elbows are medium radius (90°) with a pressure loss coefficient (k_v) of 0.8. Tee junctions operate in two modes: one acting as a 90° aggressive elbow ($k_v = 1.3$), and another where flow remains in line with the exit ($k_v = 0.05$). Valves are primarily used for ON/OFF flow control, the k_v corresponds to 0.2 for a fully open configuration.

Table 2: Components and fitting numbers for the different circuits

Circuit	Mode	L_{pip} [m]	$N_{elbows}[-]$	$N_{tee}[-]$	$N_{valves}[-]$
1	HP	12	12	4	2
	ORC	12	14	3	2
2	ORC	15	10	2	2
3	ORC	10	8	2	2
	HP	18	12	2	2

Finally, the overall ORC efficiency (η_{orc}) is determined by using equation 6, which considers the expander power output ($\dot{W}_{exp}$), the power consumption of the refrigerant pump ($\dot{W}_{pp,orc}$), and the power required by the secondary fluid pumps. Additionally, the heat extracted in the evaporator ($\dot{Q}_{ev}$) represents the energy drawn from the heat source (heat storage).

$$\eta_{orc} = \frac{\dot{W}_{exp} - \dot{W}_{pp,orc} - \sum \dot{W}_{pp,i,sf}}{\dot{Q}_{ev}} \quad (6)$$

The coefficient of performance (COP) for the HP mode is defined in equation 7, which accounts for the condenser heat power ($\dot{Q}_{cd}$), the compressor ($\dot{W}_{cp}$) and the energy consumption by the secondary fluid pumps.

$$COP = \frac{\dot{Q}_{cd}}{\dot{W}_{cp} + \sum \dot{W}_{pp,i,sf}} \quad (7)$$

3 RESULTS AND DISCUSSION

Figure 3 presents the system model, with the key variables under investigation highlighted in red boxes. These variables are systematically varied and controlled throughout the simulation process. They include the temperature glides in both the condenser and evaporator under two operating modes, as well as the supply conditions dictated by storage temperatures and the underground storage.
In contrast, other input parameters are held constant throughout the simulations to isolate the effects of the variables under study.

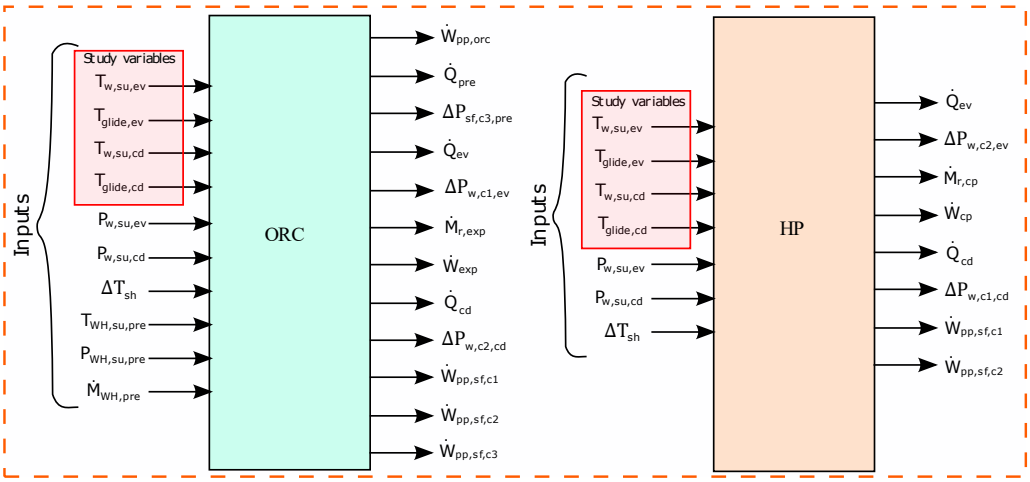

Figure 3: Modelling interaction and manipulation variables

In ORC mode, the mass flow rate in the preheater is fixed at 14 kg/s (circuit 3), which aims to represent the low-temperature waste heat available. For the ORC, the water temperature ranges from 75 to 115°C, while the fluid supply to the condenser varies from 10°C to 20°C. The preheater supply temperature is fixed at 50°C. In HP operation, the secondary fluid temperature in the condenser ranges from 70°C to 110°C, while in the evaporator, it varies between 45°C and 55°C. For these conditions, different glides are assessed.

- ORC: $T_{glide,cd}$ and $T_{glide,ev}$ are varied from 3 to 15 K with a step of 2 K.
- HP: T_{glide_cd} and $T_{glide,ev}$ are varied from 3 to 13 K with a step of 2 K.

3.1 ORC mode

Figure 4 presents the ORC efficiency by the points and the net power (considering the secondary fluid consumption) produced by the lines ($\dot{W}_{net}$) as a function of different glide combinations for three operational conditions. The performance of the machine is significantly influenced by the secondary fluid glide, leading to two main phenomena.

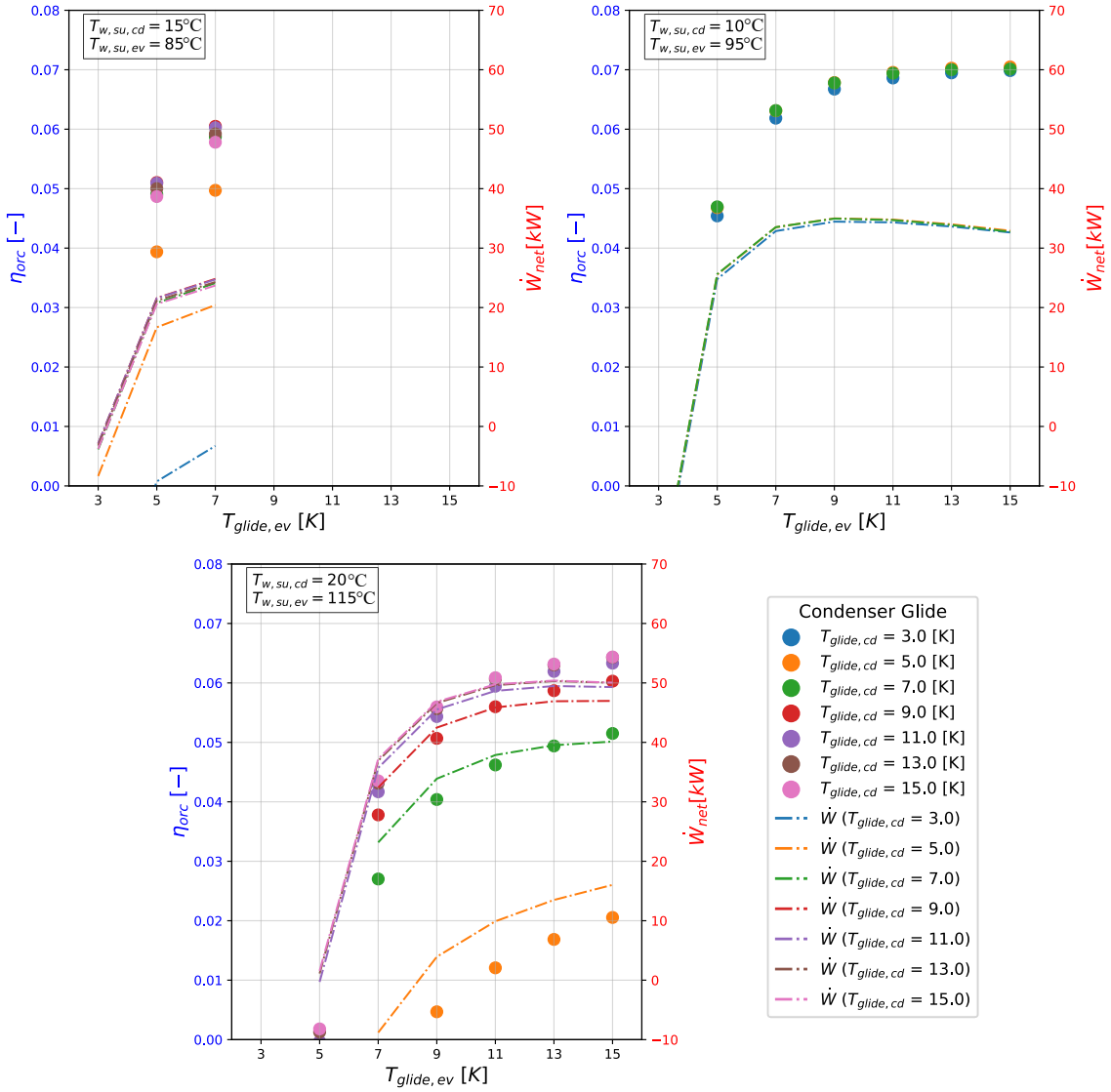

Figure 4: Glide effect on the ORC mode for three different conditions.

The first one corresponds to the larger glides, which generate a lower saturation temperature in the evaporator and bigger saturation pressures in the condenser, resulting in a lower power production. Additionally, this limits the available set of glides that can be chosen, as some conditions will not be inside of the operational envelope of the expander (provided by the manufacturer). Secondly, the

smaller glides cause a considerable increase in the secondary fluid power consumption. This happens because the mass flow rate of the secondary fluid increases significantly, sometimes even surpassing the expander power output. As a result, the system efficiency drops to negative net power.

Figure 4 also illustrates the limitations imposed by considering the real machine's influence on the results. For example, at $T_{w,su,cd} = 15°C$ and $T_{w,su,ev} = 85°C$, the system performance is primarily constrained by the evaporation temperature, which is too low. As a result, only small temperature glides in the evaporator can operate effectively, while almost all condenser glides yield viable results. In contrast, at $T_{w,su,cd} = 10°C$ and $T_{w,su,ev} = 95°C$, the primary limitation is the condensing temperature, allowing all evaporator glides to be suitable. However, for the condenser glide, only very small values are suitable. Figure 5 presents the expander envelope within the assessed operational conditions and their glides.

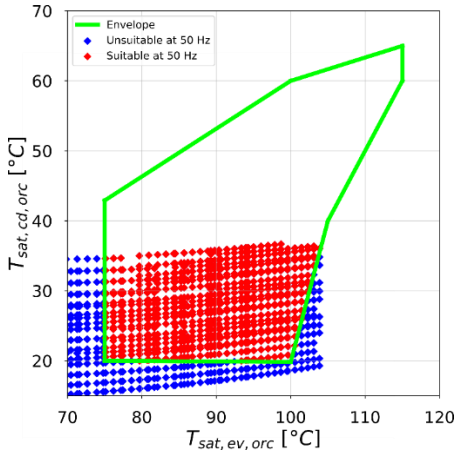

Figure 5: Operational envelope of the expander and the filtered glide conditions for an expander speed of 50 Hz.

Figure 6 presents the optimal glide for the different operational conditions. It can be observed that the optimal evaporator glide temperature increases with higher supply temperatures. Notably, after reaching $T_{w,su,ev} = 90°C$, the evaporator glide stabilises at its maximum value of 15°C. Similarly, the condenser glide also increases as the evaporator water supply temperature rises. However, this increase is less pronounced than in the evaporator. Additionally, it can be seen that for glides of 11K, 13K, and 15K, the efficiency difference is not significant, as illustrated in Figure 5. This behaviour is related to a trade-off in decreasing the internal pressure ratio, which affects both expander power ($\dot{W}_{exp}$) and secondary fluid power consumption ($\dot{W}_{sf,pp}$). Therefore, another possible criterion could be the storage discharge strategy: discharge quickly at a lower efficiency or discharge more slowly but with higher efficiency.

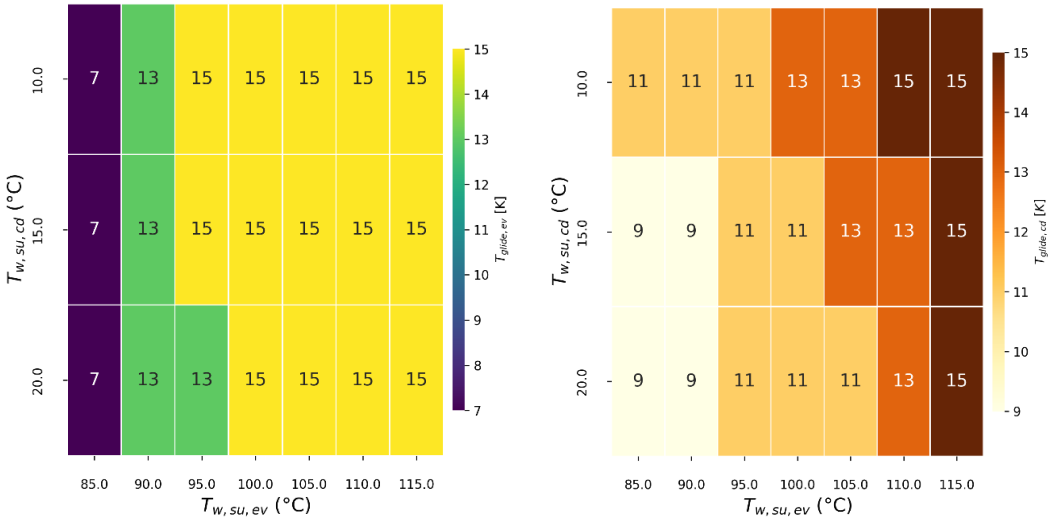

Figure 6: Optimal glides for the ORC mode (evaporator left, condenser right)

3.2 HP mode

Figure 7 presents the effect of the temperature glides on the performance by the points and consumption of the secondary fluid ($\dot{W}_{sf,pp}$) by the lines for 3 different operating conditions. The COP can take values from 2 to values higher than 6. This difference is obtained due to the isentropic efficiency of the compressor, which varies according to the pressure ratio (r_p), with higher values leading to lower isentropic efficiency, resulting in a lower COP. The operating points for the HP are within the operating envelope of the compressor. This means that for the conditions evaluated, all glides can be valid operating combinations. The COP value reaches a maximum and then begins to decrease as the evaporator glide increases. This value changes for evaporator slip, 7K for the first condition, 5K for the second and 3K for the third, even though the energy of the secondary fluid pumps decreases as the glides increase. Regarding the thermal power, this decreases as the glide increases. Therefore, to reduce the charging time of a reservoir, thermal power should be prioritised over efficiency. This is especially important when considering integration with surplus energy from the grid, which can be considered as a "free energy source".

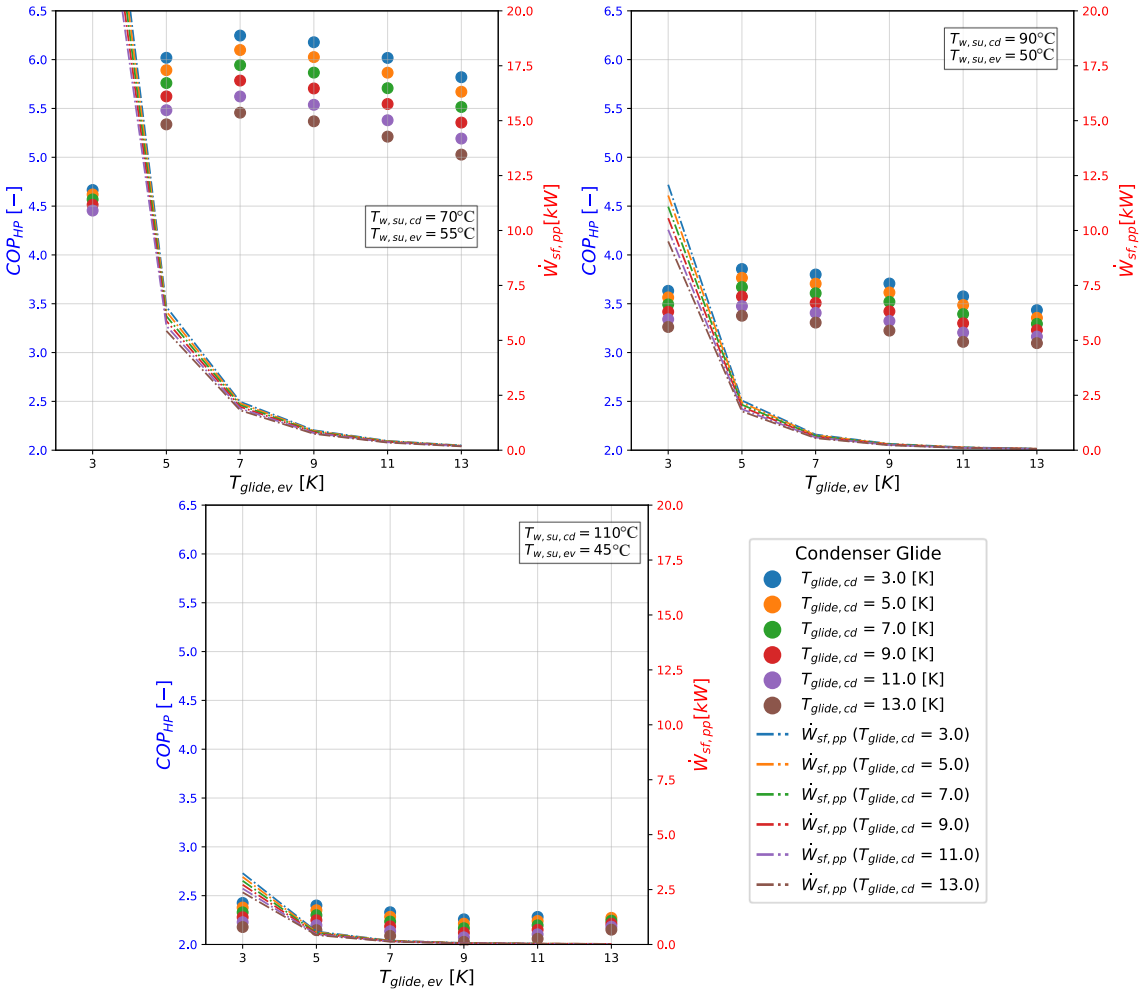

Figure 7: Glide effect on the HP mode for 3 different conditions.

Figure 8 presents the optimal glide values for maximum COPs at various operating conditions. These variations highlight the need to apply an effective control strategy, as the optimal glide conditions differ significantly from one condition to another. Additionally, these glides are quite different from those required for the ORC (Figure 6). This means that the selected pump must be able to operate in both modes for different flow and head conditions. Therefore, a frequency drive is essential for the secondary circuits of the CB.

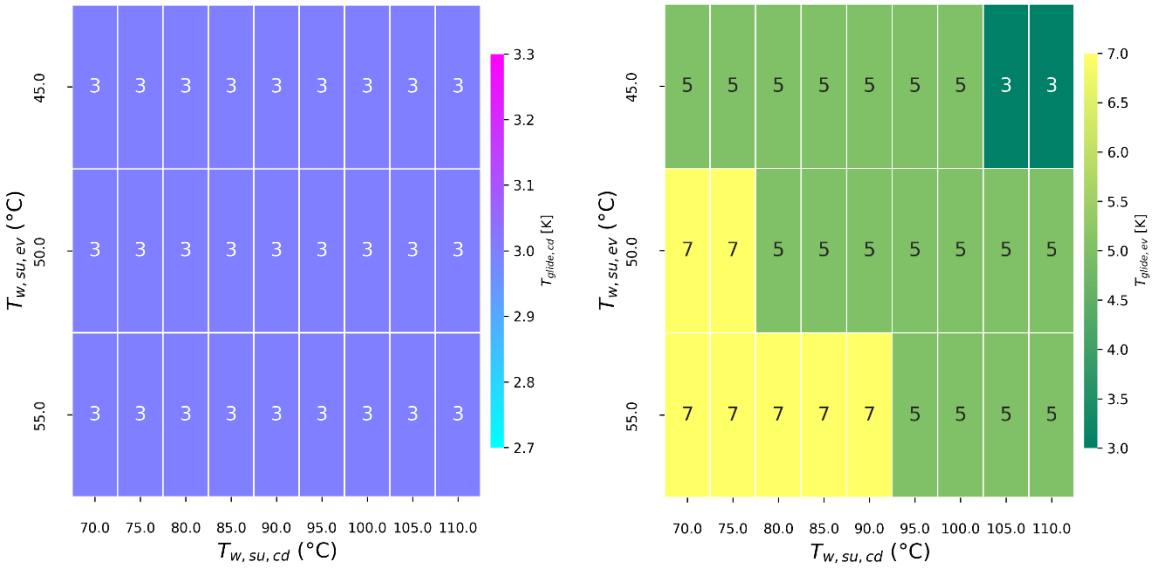

Figure 8: Optimal glides for the HP mode (condenser left, evaporator right)

4 CONCLUSIONS

This study presents the case of a 50 kWe and 500 kWth CB currently under development at the University of Liège as part of the WeForming project. This model incorporates the effects of actual components and pipe configurations to determine optimal operating conditions. The results indicate that no single combination of glides for the evaporator and condenser provides optimal performance in both ORC and HP operating modes. The net performance of the system is highly sensitive to the integration of the secondary fluid. Generating a balance between the mass flow rate of the secondary fluid and the pressure drops in the circuits. Excluding the effect of secondary fluid in CB can have a considerable impact on performance analysis, as optimisation would tend to focus exclusively on maximising the pressure lift in the ORC cycle and the optimum pressure ratio for the HP. This approach can lead to excessive energy consumption associated with secondary fluids, resulting in a net penalty in the overall system efficiency rather than an improvement. The key findings of this study can be summarised as follows:

- Higher temperature glides reduce secondary fluid pump consumption; however, beyond a certain threshold, this effect stabilises, producing no significant further reduction. For ORC, the average optimal glides correspond to 11K and 15K for the condenser and evaporator, respectively. Meanwhile, the average optimal glides for HP correspond to 3K and 5K for the condenser and evaporator, respectively.
- Similar trends apply to other CBs, but the optimal glide values could differ due to system-specific factors such as piping diameter (DN100) and the chosen expander/compressor.
- The accuracy of the results could be improved by using smaller glide steps to refine the control map. However, adjustments must remain within a feasible range, as both ORC and HP modes utilise the same secondary fluid circuits and pump.
- Different optimisation strategies can be explored, such as improving charging and discharging times based on the energy produced or consumed.

Further investigation is required to determine whether a pump configuration is suitable for both ORC and HP modes. Indeed, the glides are quite different in both modes, which can lead the HP cycle to present a larger head height for the same volumetric flow. If not, alternative solutions should be considered, such as pumps capable of handling low head heights and high volumetric flows or circulators to assess their feasibility.

REFERENCES

Ahmadfard, M., & Baniasadi, E. (2025). Borehole thermal energy storage systems: A comprehensive review using bibliometric and qualitative tools. *Applied Energy*, *387*, 125638. https://doi.org/10.1016/j.apenergy.2025.125638

Amalfi, R. L., Vakili-Farahani, F., & Thome, J. R. (2016a). Flow boiling and frictional pressure gradients in plate heat exchangers. Part 1: Review and experimental database. *International Journal of Refrigeration*, *61*, 166–184. https://doi.org/10.1016/j.ijrefrig.2015.07.010

Amalfi, R. L., Vakili-Farahani, F., & Thome, J. R. (2016b). Flow boiling and frictional pressure gradients in plate heat exchangers. Part 2: Comparison of literature methods to database and new prediction methods. *International Journal of Refrigeration*, *61*, 185–203. https://doi.org/10.1016/j.ijrefrig.2015.07.009

Bell, I. H., Wronski, J., Quoilin, S., & Lemort, V. (2014). Pure and Pseudo-pure Fluid Thermophysical Property Evaluation and the Open-Source Thermophysical Property Library CoolProp. *Industrial & Engineering Chemistry Research*, *53*(6), 2498–2508. https://doi.org/10.1021/ie4033999

Cendoya, A., Ransy, F., Lemort, V., Dumont, O., Guo, B., & Dewallef, P. (2024c). Numerical Modelling of a 50 kWe reversible Carnot Battery coupled with waste heat. 1st Belgian Symposium of Thermodynamics. 1st Belgian Symposium of Thermodynamics, Liège, Belgium.

Cendoya, A., Ransy, F., Lemort, V., Hernandez, A., Gresse, P.-H., & Windeshausen, J. (2024b). Modelling and Simulation of a Carnot Battery Coupled to Seasonal Underground Stratified Thermal Energy Storage for Heating, Cooling and Electricity Generation. *International High Performance Buildings Conference*, 10. https://docs.lib.purdue.edu/ihpbc/472/

Cendoya, A., Ransy, F., Lemort, V., Kozlowska, N., & Dewallef, P. (2024a). Modelling and Simulation of a Seasonal Underground Water Storage Coupled With Photovoltaic Panels, Heat Pump and District Heating Network for Providing Local Renewable Heating to a Residential District. *37th International Conference on Efficiency, Cost, Optimization, Simulation and Environmental Impact of Energy Systems (ECOS 2024)*, 12. https://doi.org/10.52202/077185-0124

Cioncolini, A., & Thome, J. R. (2012). Void fraction prediction in annular two-phase flow. *International Journal of Multiphase Flow*, *43*, 72–84. https://doi.org/10.1016/j.ijmultiphaseflow.2012.03.003

Cuevas, C., Lebrun, J., Lemort, V., & Ngendakumana, P. (2009). Development and validation of a condenser three zones model. *Applied Thermal Engineering*, *29*(17–18), 3542–3551. https://doi.org/10.1016/j.applthermaleng.2009.06.007

Cuevas, C., Lebrun, J., Lemort, V., & Winandy, E. (2010). Characterization of a scroll compressor under extended operating conditions. *Applied Thermal Engineering*, *30*(6–7), 605–615. https://doi.org/10.1016/j.applthermaleng.2009.11.005

Daniarta, S., Kolasiński, P., & Imre, A. R. (2024). Performance map and theoretical analysis of Carnot battery technology via novel reversible Rankine-based cycle. *Energy Reports*, *11*, 4500–4514. https://doi.org/10.1016/j.egyr.2024.04.024

Dehghani-Sanij, A. R., Tharumalingam, E., Dusseault, M. B., & Fraser, R. (2019). Study of energy storage systems and environmental challenges of batteries. *Renewable and Sustainable Energy Reviews*, *104*, 192–208. https://doi.org/10.1016/j.rser.2019.01.023

Eck, B. (1973). *Fans: Design and operation of centrifugal, axial-flow and cross-flow fans* (1. engl. ed). Pergamon Pr.

Guo, B., Lemort, V., & Cendoya, A. (2025). Control Strategy and Techno-economic Optimization of a Small-scale Hybrid Energy Storage System: Reversible HP/ORC-based Carnot Battery and Electrical Battery. *Energy*, 136508.

Hodge, B.-M., Brancucci Martinez-Anido, C., Wang, Q., Chartan, E., Florita, A., & Kiviluoma, J. (2018). The combined value of wind and solar power forecasting improvements and electricity storage. *Applied Energy*, *214*, 1–15. https://doi.org/10.1016/j.apenergy.2017.12.120

Holger Martin (Ed.). (2010). N6: Pressure Drop and Heat Transfer in Plate Heat Exchangers. In *VDI HeatAtlas: Chapter*. Springer Berlin Heidelberg. https://doi.org/10.1007/978-3-540-77877-6

International Energy Agency (IEA). (2024). *Renewable 2024 Analysis and forecast to 2030* (p. 177). https://www.iea.org/reports/renewables-2024,

Kast, W., Nirschl, H., & Gaddis, E. (2010). L1 pressure drop in single phase flow. In *VDI HeatAtlas: Chapter* (2nd Ed., pp. 1053–1116). https://link.springer.com/referenceworkentry/10.1007/978-3-540-77877-6_70

Lemort, V., Declaye, S., & Quoilin, S. (2012). Experimental characterization of a hermetic scroll expander for use in a micro-scale Rankine cycle. *Proceedings of the Institution of Mechanical Engineers, Part A: Journal of Power and Energy*, *226*(1), 126–136. https://doi.org/10.1177/0957650911413840

Longo, G. A. (2010). Heat transfer and pressure drop during HFC refrigerant saturated vapour condensation inside a brazed plate heat exchanger. *International Journal of Heat and Mass Transfer*, *53*(5–6), 1079–1087. https://doi.org/10.1016/j.ijheatmasstransfer.2009.11.003

Martin, H. (1996). A theoretical approach to predict the performance of chevron-type plate heat exchangers. *Chemical Engineering and Processing: Process Intensification*, *35*(4), 301–310. https://doi.org/10.1016/0255-2701(95)04129-X

McTigue, J., Hirschey, J., & Ma, Z. (2025). Advancing pumped thermal energy storage performance and cost using silica storage media. *Applied Energy*, *387*, 125567. https://doi.org/10.1016/j.apenergy.2025.125567

Pinto, M. T., Žibret, G., Lopes, L., Bodo, B., & Zajzon, N. (2020). UNEXUP: Robot-based exploration technology for underground flooded mines. *Advances in Geosciences*, *54*, 109–117. https://doi.org/10.5194/adgeo-54-109-2020

Ritchie, H., Rosado, P., & Roser, M. (2024). Electricity mix. *Our World in Data*. https://ourworldindata.org/electricity-mix

Shah, M. M. (2021). Heat transfer during condensation in corrugated plate heat exchangers. *International Journal of Refrigeration*, *127*, 180–193. https://doi.org/10.1016/j.ijrefrig.2021.02.011

Vecchi, A., Knobloch, K., Liang, T., Kildahl, H., Sciacovelli, A., Engelbrecht, K., Li, Y., & Ding, Y. (2022). Carnot Battery development: A review on system performance, applications and commercial state-of-the-art. *Journal of Energy Storage*, *55*, 105782. https://doi.org/10.1016/j.est.2022.105782

Virtanen, P., Gommers, R., Oliphant, T. E., Haberland, M., Reddy, T., Cournapeau, D., Burovski, E., Peterson, P., Weckesser, W., Bright, J., Van Der Walt, S. J., Brett, M., Wilson, J., Millman, K. J., Mayorov, N., Nelson, A. R. J., Jones, E., Kern, R., Larson, E., … Vázquez-Baeza, Y. (2020). SciPy 1.0: Fundamental algorithms for scientific computing in Python. *Nature Methods*, *17*(3), 261–272. https://doi.org/10.1038/s41592-019-0686-2

ACKNOWLEDGEMENT

The project that produced the results presented in this paper has received funding from the European Union's Horizon Research and Innovation programme under grant agreement No. 10112355, in the framework of the WeForming project. The authors would also like to acknowledge the funding provided by the Walloon Region of Belgium in the framework of the ARDNrgy project.